Evidence of Noncollinear Spin Texture in Magnetic Moiré Superlattices

Hongchao Xie[1,+], Xiangpeng Luo[1,+], Zhipeng Ye[2,+], Zeliang Sun[1,+], Gaihua Ye[2], Suk Hyun Sung[3], Haiwen Ge[4], Shaohua Yan[5], Yang Fu[5], Shanjie Tian[5], Hechang Lei[5], Kai Sun[1], Robert Hovden[3], Rui He[2,*], & Liuyan Zhao[1,*]

[1] Department of Physics, the University of Michigan, 450 Church Street, Ann Arbor, MI, 48109, USA

[2] Department of Electrical and Computer Engineering, Texas Tech University, 910 Boston Avenue, Lubbock, TX, 79409, USA

[3] Department of Materials Science and Engineering, the University of Michigan, 2300 Hayward St, Ann Arbor, MI 48109, USA

[4] Department of Mechanical Engineering, Texas Tech University, 2703 7th Street, Lubbock, TX, 79409, USA

[5] Department of Physics and Beijing Key Laboratory of Opto-electronic Functional Materials & Micro-Nano Devices, Renmin University of China, Beijing, 100872, China

[*] Corresponding authors: rui.he@ttu.edu; lyzhao@umich.edu

[+] These authors contributed equally

ABSTRACT

Moiré magnetism, parallel with moiré electronics that has led to novel correlated and topological electronic states [1,2], emerges as a new venue to design and control exotic magnetic phases in twisted magnetic two-dimensional (2D) crystals. Noncollinear spin texture emerging from twisted 2D magnets with collinear spins is the most profound consequence of moiré magnetism and forms the basis for realizing novel magnetic orders and excitations. Yet, no direct experimental observation of noncollinear spins in moiré magnets have been made despite recent theoretical [3-7] and experimental [8-10] efforts. Here, we report the evidence of noncollinear spin texture in 2D twisted double bilayer (tDB) magnet chromium triiodide (CrI_3). By studying the magnetic field dependent magnetic circular dichroism (MCD) in tDB CrI_3, we distinguished the noncollinear spins with a gradual spin flop process from the collinear spins with sudden spin flip transitions, and identified a net magnetization emerging from the collinear spins. By examining the twist angle dependence, we demonstrated that both noncollinear spins and net magnetization are present at twist angles from 0.5° to 5°, but are most prominent in the 1.1° tDB CrI_3. By tracking the temperature dependent MCD of the 1.1° tDB CrI_3, we further resolved a new critical temperature of 25 K, for the onset of the net magnetization and the softening of the noncollinear spins, which is dramatically suppressed from the Néel temperature of 45 K for natural few layers. Our results establish the emergence of noncollinear spins from magnetic moiré superlattices and provide a versatile platform to explore nontrivial magnetism with noncollinear spins.

Noncollinear magnetism covers a wealth of exotic magnetic phases in three-dimensional (3D) bulk systems, for example, chiral antiferromagnetism [11], spiral magnetism [12], helical magnetism [13], skyrmions [14], magnetic multipoles [15] etc, many of which hold promise for spintronic applications. It has been demonstrated that magnetic competition, where competing forces for opposite spin alignments cannot be simultaneously satisfied, is one venue to introduce noncollinear spin texture. Down to the two-dimensional (2D) limit, all the discovered 2D magnets, both ferromagnetic and antiferromagnetic ones, thus far only host collinear spins [16-21]. Enlighten by moiré electronics where new electronic phases emerge due to the presence of moiré superlattices [1,2], the magnetic analogue, moiré magnets made by twisting two magnetic atomic layers, is expected to introduce emergent magnetic phases that are distinct from those in natural 2D magnets. An immediate, interesting topic in this context is whether 2D noncollinear spin texture can be introduced in moiré superlattices made of twisted 2D magnets with collinear spins. Very recently, this scenario has been theoretically predicted in moiré magnets where stacking dependent interlayer exchange couplings with opposite signs coexist and compete within individual moiré supercells [3-7]. However, the experimental observation and characterization of moiré-induced 2D noncollinear spin texture remain absent despite a few very recent efforts of probing coexisting magnetic orders in twisted chromium triiodide (CrI_3) layers [8-10].

CrI_3 has an out-of-plane easy axis for the ferromagnetic (FM) intralayer exchange coupling [22], and thus its long-range magnetic order survives down to the atomic layer limit [23]. Extensive experiments [24-26] and calculations [27-29] have shown that monoclinic interlayer stacking leads to antiferromagnetic (AFM) interlayer exchange coupling whereas rhombohedral interlayer atomic registry results in FM interlayer exchange coupling. In natural few-layer CrI_3, the structure favors the monoclinic stacking, and consequently the magnetism takes the layered AFM order where spins align along the same out-of-plane direction within the layers but in opposite directions between adjacent layers [23]. Importantly, even-layer CrI_3 has a compensated zero magnetization whereas odd-layer CrI_3 ends up with a finite non-zero magnetization. In twisted double odd-layer CrI_3, regions with zero and non-zero magnetization coexist at small twist angles [9,10]; and in twisted double even-layer CrI_3, an unexpected non-zero magnetization emerges around a critical twist angle of 1.1^o [8]. Yet, the question of spin reorientation, upon moiré modulations, to depart from the collinear arrangement in natural layers remains unexplored in these three pioneering experimental works.

Here, we choose the twisted double bilayer (tDB) CrI_3 system to show and characterize the noncollinear spins from the moiré engineering. The tDB CrI_3 is an artificial four-layer homostructure made by two bilayer (2L) CrI_3 stacked vertically with a controlled twist angle α, as shown in the inset of Fig. 1a. At the interface between the two bilayers, a moiré superlattice develops that consists of overlying (AA),

rhombohedral (R), and monoclinic (M) stackings within individual moiré supercells (marked as green, blue, and red sites within the black parallelogram, respectively, in Fig. 1a). Based on first principle calculations [27], a periodically modulating interlayer exchange coupling of moiré wavelength forms between the 2nd and 3rd layers (*i.e.*, between the two bilayers), with nearly no coupling at the AA sites, ~ 0.04 meV/μ_B^2 AFM interlayer coupling at the M sites, and ~ – 0.6 meV/μ_B^2 FM interlayer coupling at R sites, as shown in Fig. 1b. This interlayer moiré exchange coupling that periodically varies from AFM- to FM-type prefers to have spatially modulating spin arrangement, whereas the intralayer FM exchange coupling favors uniform out-of-plane spin alignment within a CrI_3 layer. It is the competition between these two exchange couplings that determines the magnetic ground state in tDB CrI_3.

Using a continuous spin model (see Methods), we compute the total magnetic energy of the system that includes intralayer FM coupling, uniform interlayer AFM coupling within each bilayer, and interlayer moiré exchange coupling between the two bilayers, and identify the ground state spin configuration by minimizing this magnetic energy. We find that the magnetic ground state evolves as the twist angle increases and the computed results at three representative twist angles (0.1°, 1°, and 10°) are shown in Fig. 1c-e. At very small twist angles like 0.1° in Fig. 1c, spatially modulating out-of-plane magnetization m_z develops in both the 1st and 2nd layers and is antiparallel between these two layers, whereas homogeneous m_z forms in the 3rd and 4th layers with spin up (↑, $m_z = 3\mu_B$) in layer 3 and spin down (↓, $m_z = -3\mu_B$) in layer 4. We further correlate the layered magnetism with the lattice stacking in Fig. 1f. The islands centering at AA stacking and surrounded by M stacking take the ↑↓↑↓ layered magnetic order, and the large remaining region centering at R stacking has the ↑↓↓↑ layered magnetism. The boundaries between the two regions in the top bilayer exhibits the noncollinear spin texture (↘↗ in layer 1 and ↗↘ in layer 2). Summing m_z in all four layers for this magnetic ground state of 0.1° tDB CrI_3 leads to zero total magnetization ($M_z^{0.1^o} = 0$). At intermediate twist angles such as 1°, the computed magnetic ground state in Fig. 1d shows modulated spins only in the 2nd layer and a net total magnetization ($M_z^{1^o} \neq 0$), which features islands with nonzero magnetization (↑↑↓↑) centering at AA sites, boundaries with noncollinear spins in layer 2 coinciding with the rings formed by M sites, and a background with zero magnetization (↑↓↓↑) primarily centering at R sites. At large twist angles like 10°, the calculated result shows homogenous spins within all four layers in Fig. 1e and takes the ↑↓↓↑ layered magnetic order with total zero magnetization ($M_z^{10^o} = 0$) in Fig. 1h. While the details of the spin configurations may vary depending on the microscopic parameters in the model, the emergence of nonzero magnetization only at intermediate twist angles and the formation of noncollinear spins in small to intermediate twist angles are robust features in our simulated moiré magnetism in tDB CrI_3 (see detailed discussions on the twist angle dependence in Supplementary Information).

To connect the theoretical calculations to experimental measurements, we first establish that our tDB CrI_3 host high-quality moiré superlattice, using selected area electronic diffraction (SAED) and dark-field transmission electron microcopy (DF-TEM) (see Methods). Figure 2a shows the electron diffraction pattern of a tDB CrI_3 with a twist angle of $\alpha = 1.4^{o} \pm 0.1^{o}$. In addition to three pairs of Bragg peaks from the CrI_3 honeycomb lattice ($\bar{3}300$, $0\bar{3}30$, and $30\bar{3}0$, marked by the two black circles for the $\bar{3}300$ pair), we can also observe two additional peaks locating between each pair (marked by the two blue circles between the $\bar{3}300$ pair), which correspond to the 2nd order moiré superlattice peaks. This clear observation of superlattice peaks in the diffraction pattern is strong and direct evidence of the formation of moiré superlattices [30]. Figure 2b shows the real space DF-TEM images for the three pairs of Bragg and superlattice peaks, labeled by the corresponding Bragg peak indices. Consistent with the presence of superlattice peaks in the electron diffraction pattern, the DF-TEM image for every pair clearly shows the parallelogram feature, in contrast to parallel lines for the case without superlattice formation. Figure 2c is the composite image made by summing up the three DF-TEM images in Fig. 2b, which clearly shows the superlattice structures uniformly extending across the field of view, an area of ~ 250×125 nm^2. We note that this superlattice wavelength is $1/\sqrt{3}$ of the moiré wavelength, because this superlattice is imaged from the 2nd order superlattice peaks, which is $\sqrt{3}$ times of the moiré wavevector. The presence of uniform, high-quality moiré superlattice in our tDB CrI_3 lays a solid foundation for us to look for emergent magnetic properties from them.

Having shown the high-quality moiré superlattice in tDB CrI_3, we use magnetic circular dichroism (MCD) to directly verify the non-zero magnetization and its magnetic field dependence to reveal the noncollinear spin texture (see Methods). Figure 3a shows the MCD data as a function of an out-of-plane magnetic field ($B_\perp$) swept from + 2T to – 2T and then back to + 2 T, taken on a 1.1° tDB CrI_3 (top panel), as well as a 2L (middle panel) and a 4L (bottom panel) CrI_3 as reference. Two outstanding features are observed from the comparison between the datasets of the 1.1° tDB and natural 2L/4L CrI_3, despite similar spin flip transitions at $B_{c1}^{tDB} = \pm 0.67$T to those at $B_{c1}^{2L} = \pm 0.73$T [23] and $B_{c1}^{4L} = \pm 0.82$T [31,32]. First, in the 1.1° tDB CrI_3, the MCD values at $B_\perp = 0$T are nonzero, and the magnetic field dependence shows a clear hysteresis loop between B_{c1}^{tDB}, which is in sharp contrast to the nearly zero MCD values and absence of hysteresis between $B_{c1}^{2L/4L}$ in 2L/4L CrI_3. Second, for the 1.1° tDB CrI_3, the MCD data show gradual increase (i.e., positive slopes) both between and beyond B_{c1}^{tDB}, which is clearly distinct from the plateaus of constant MCD values (i.e., zero slopes) outside of the spin flip transition fields for 2L and 4L CrI_3. We note that the nonzero MCD at 0T and the hysteresis loop between B_{c1}^{tDB} are strong and direct evidence for a net magnetization in the 1.1° tDB CrI_3, as expected from the non-compensated magnetized islands with a net nonzero $M_z^{1.1^o}$ in

Fig. 1d. We highlight that the gradual increase in MCD outside of B_{c1}^{tDB} suggests the presence of spin flop process and thus noncollinear spins in the 1.1° tDB CrI_3, consistent with the in-plane spin moments at the boundaries between the islands and background in Fig. 1d.

We can then model and fit the MCD data of the 1.1° tDB CrI_3 with two major contributions – one from the collinear spins that feature the sharp spin flip transitions and the other from the noncollinear spins that account for the gradual spin flop process (see Methods). The fitted results are shown in Figs. 3a (solid lines), 3b and 3c for the sum and each of the contributions in the 1.1° tDB CrI_3 (top panels), together with those for 2L and 4L CrI_3 (middle and bottom panels). This fit is independent from but consistent with the simulations in Fig. 1d in terms of the following two key aspects. First, the net magnetization falls into the collinear spin contribution in this fit (Fig. 3b, top panel), matching the magnetized islands with collinear ↑↑↓↑ spin arrangements in the simulations (Figs. 1d and 1g). Second, for the noncollinear spin contribution, the two fitted MCD traces (Fig. 3c, top panel) with decreasing and increasing $B_\perp$ overlap with each other within our fit uncertainties, echoing the computed net zero out-of-plane magnetization at the boundaries between the ↑↑↓↑ islands and the ↑↓↑↓ background in Fig. 1d. As a controlled comparison, the fits for 2L and 4L CrI_3 are dominated by the collinear spin contribution with compensated magnetizations below $B_{c1}^{2L/4L}$ (Fig. 3b, middle and bottom panels) and show tiny noncollinear spin contributions (Fig. 3c, middle and bottom panels). We comment that the tiny noncollinear contributions in 2L/4L CrI_3 possibly arise from very small but finite thermal fluctuations at our measurement temperature 10K.

Based on the computations and the fit, we further provide a physics picture of spin texture evolution upon $B_\perp$ to vividly interpret the MCD data. In Fig. 3d, we start with the computed ground state for the 1.1° tDB CrI_3 at 0T (step I) and depict the evolution of spin states under increasing $B_\perp$ till 2T. Initially, with $B_\perp$ smaller than B_{c1}^{tDB}, the boundaries with noncollinear spins in the 2nd layer gradually move outwards to expand the ↑↑↓↑ islands because the upwards $B_\perp$ direction aligns along the spin up orientation for the island in this 2nd layer (step II). This process accounts for the slow increase of MCD below B_{c1}^{tDB}. Right across B_{c1}^{tDB}, the collinear spins in the background region flip from ↑↓↓↑ to ↑↑↑↑, which concurrently shifts the modulating spin structure from the 2nd to the 3rd layer (step III). This change, responsible for the sharp jump in MCD at B_{c1}^{tDB}, happens because it costs the energy penalty of interlayer exchange coupling with one adjacent layer that B_{c1}^{tDB} can afford. It is similar to the cases of spin flip transitions for 2L CrI_3 and for the outer most layer in 4L CrI_3 with $B_{c1}^{2L/4L}$ that is close to B_{c1}^{tDB}. With further increasing $B_\perp$, the boundaries with noncollinear spins in the 3rd layer move inwards to shrink the ↑↑↓↑ islands where the upwards $B_\perp$ points in the opposite direction to the downwards spins in the islands in this 3rd layer (step IV). This evolution explains the further gradual increase of MCD above B_{c1}^{tDB}. Eventually, the islands in the 3rd layer

disappear, and spins in all four layers of tDB CrI_3 are polarized to the same direction as $B_\perp$ (step V). This final state corresponds to the saturation of MCD, which should happen at $B_\perp$ close to or smaller than B_{c2}^{4L}.

Having established the analysis and interpretation of MCD data for the 1.1° tDB CrI_3, we proceed to explore the twist angle dependence of the moiré magnetism. Figure 4a displays the raw MCD data (top panel) normalized to values at 2T, together with the fits for the sum (top panel) and each (middle and bottom panels) of contributions from collinear and noncollinear spins, for 4L, $\alpha = 0.5°$, 1.1°, 2°, 5°, 10° tDB, and 2L CrI_3 (see the raw data without normalization in Supplementary Information). A general trend can be seen that the MCD data resemble 4L CrI_3 at very small twist angles (e.g., 0.5°) in having two spin flip transitions, then distinguish from either 4L or 2L CrI_3 at intermediate twist angles (e.g., 1.1°, 2°, and 5°) by showing a significant hysteresis loop as well as an appreciable noncollinear spin contribution, and eventually converge to 2L at large twist angles (e.g., 10°). To better quantify this trend, we plot the twist angle dependence of five important parameters extracted from the fits, namely, the spin flip transition field B_{c1} that corresponds to the interlayer coupling within each bilayer (Fig. 4b), the width of the spin flip transitions ΔB_{c1} that describes the spatial inhomogeneity from moiré magnetism (Fig. 4c), the slope at 0T $\Delta\mathrm{MCD}/\Delta B_\perp(0\mathrm{T})$ that depicts the susceptibility of the noncollinear spins (Fig. 4d), the ratio of the noncollinear spin contribution to the total MCD $W_{noncollinear}$ that scales with the weight of the noncollinear spins (Fig. 4e), and the magnitude of net magnetization M_z^{tDB} that is not expected in 2L, 4L, and any homogeneous stacking of two 2L CrI_3 [8] (Fig. 4f). A minimum in B_{c1} at 1.1° in Fig. 4b shows that the moiré interlayer coupling between the two bilayers indeed modifies the uniform interlayer coupling within each bilayer and maximizes this impact at 1.1°. A maximum of ΔB_{c1} however happens at 0.5° in Fig. 4c, most likely resulted from the extra 4L-like region (↑↓↑↓) within moiré supercells which is marked by the presence of B_{c2} in the 0.5° tDB CrI_3 and is proven to be absent in tDB CrI_3 of higher twist angles, in addition to the ↑↑↓↑ and ↑↓↓↑ regions. The slope of tDB CrI_3 obviously departs from those of 2L and 4L CrI_3 and peaks at 1.1°, which is evident of the moiré induced softening for noncollinear spins that lie at the boundaries between collinear spin regions with opposite spin directions. The noncollinear spin contribution maximizes at 1.1°, further suggesting the optimal moiré magnetism for tDB CrI_3 around this twist angle. And lastly, the nontrivial net magnetization, that only develops upon twisting between two bilayer CrI_3, clearly peaks at 1.1°. Its systematic nonmonotonic twist angle dependence being consistent with those of B_{c1}, $\Delta\mathrm{MCD}/\Delta B_\perp(0\mathrm{T})$, and $W_{noncollinear}$ well demonstrates the key role of twist angle, or equivalently moiré wavelength, in the emergent magnetic properties in tDB CrI_3.

For the optimal twist angle 1.1° tDB CrI_3, we further carry out the temperature dependence measurement of MCD data from 60 K to 10 K, across the Néel temperature $T_N = 45\mathrm{K}$ for natural few-layer CrI_3. Figure

5a shows the raw data and fits of MCD datasets at selected temperatures for 1.1° tDB CrI_3 (see raw data for 2L and 4L CrI_3 in Supplementary Information). At 60K, the MCD data show a linear dependence on $B_\perp$ and confirms the paramagnetic behavior at this temperature. Below 40K, the spin flip transitions at B_{c1}^{tDB} become progressively visible, and furthermore, at 25K, the hysteresis loop with nonzero MCD at 0T appears. We first discuss the fitting parameters for the collinear spin contribution (Figs. 5b–5d). The fitted values for MCD at 0T spectra kick up at around 25K (Fig. 5b), which is significantly reduced from the onset of around 45K for the layered AFM in 2L/4L CrI_3 [31]. Temperature dependent B_{c1} for the 1.1° tDB CrI_3 follows the same trend as those for 2L/4L CrI_3 and shows an onset around 45K (Fig. 5c). The temperature dependence of ΔB_{c1} for the 1.1° tDB CrI_3 clearly departs from those for 2L/4L CrI_3 at temperatures below about 25K when the net magnetization in the ↑↑↓↑ islands build up. We then move on to the fitting parameters for the noncollinear spin contribution (Figs. 5e and 5f). The temperature dependence of the slope peaks (or even diverges) around 45K for both the 1.1° tDB and natural 2L/4L CrI_3, but it has a much larger magnitude in tDB than 2L/4L CrI_3 below 45K (Fig. 5e). The temperature dependence of $W_{noncollinear}$ below 45K shows a decreasing trend for both 1.1° tDB and 2L/4L CrI_3 as the thermal excitation-induced spin canting gets suppressed at lower temperatures. But $W_{noncollinear}$ of 1.1° tDB CrI_3 is much greater than those of 2L and 4L CrI_3, and further shows a steeper decrease below about 25K when the net magnetization shows up.

Through temperature dependent MCD fitting parameters, two characteristic temperatures, T_{c1} = 45K and T_{c2} = 25K, are revealed in 1.1° tDB CrI_3. To approach the origin of the suppressed net magnetization onset temperature of 25K, we first examined the temperature dependent MCD for tDB CrI_3 with a larger twist angle, e.g., 2°. We confirmed the 45K magnetization onset temperature in 2° tDB CrI_3 (see the results in Supplementary Information), which convincingly rules out the weakened inter-bilayer exchange coupling as the cause for the suppression in the magnetization onset temperature in 1.1° tDB CrI_3. We further performed temperature dependent polarized Raman spectroscopy measurements in 1.1° tDB CrI_3, where the layered-magnetism-assisted Raman Scattering probes the layered magnetic orders even with zero magnetization [31] and is therefore complementary to the net magnetization-sensitive MCD. Figure 5g shows Raman spectra in the linearly parallel and crossed channels at selected temperatures. In total four modes ($U_{1\text{-}4}$) are observed due to the Davydov splitting, with three in the crossed channel ($U_{2\text{-}4}$) from the layered-magnetism-assisted phonon scattering process and the rest one in the parallel channel (U_1) from the regular phonon scattering [8,31]. The fitted frequencies are very similar to those of natural 4L CrI_3 [31], suggesting excellent lattice coupling between two bilayers in 1.1° tDB CrI_3. The temperature dependence of $U_{2\text{-}4}$ intensities is plotted in Fig. 5h which clearly shows onset at 45K and corresponds to the formation of the ↑↓↓↑ layered magnetic order in the R region, in contrast to 25K arising from the net magnetization in the in

the ↑↑↓↑ islands of the M surround region. This finding of lower magnetic onset in the ↑↑↓↑ islands than in the ↑↓↓↑ background can be understood from two facts related with magnetic competitions in 1.1° tDB CrI_3: Firstly, the ↑↑↓↑ order in the M surrounded islands is a consequence of magnetic competitions and is against its naturally favored ↑↓↑↓ state, whereas the ↑↓↓↑ order in the R region simply is its preferred state; Secondly, 1.1° is closer than 2° to the critical angle across which the magnetic ground state switches from having spatially modulated spin alignment in two layers to that in one layer (Figs. 1c and 1d), therefore stronger magnetic competitions are expected in 1.1° than larger angles.

In summary, we have used electron microscopy to demonstrate the high-quality moiré superlattice in tDB CrI_3, and then magneto-optical measurements to show signatures of an emergent net magnetization and noncollinear spin texture, demonstrate impacts of moiré-induced magnetic competitions, and identify the unique twist angle of around 1.1° for this system. Because our optical studies here are limited to a micrometer resolution and thus only probe the averaged effect across a large number of moiré supercells, future studies by spin-sensitive probes with nanometer spatial resolutions are needed to visualize detailed spin textures within moiré supercells [33]. Their integration with applications of external magnetic field, if possible, will further enable research on the spin pattern evolution under $B_{\perp}$. Moreover, dynamic probes, such as time-resolved magneto-optics [34], magneto-Raman [24,35], or their near-field versions, or even inelastic x-ray scattering [36], are called for to probe moiré magnons in these moiré magnets. A combination of static spin textures and dynamic magnons can provide us with a complete picture of the moiré magnetism, which can further guide the design and application of interesting magnetic phenomena in moiré magnets.

Figure Captions

Figure 1. Calculations of the magnetic ground states of tDB CI_3. a. The moiré superlattice formed at the interface between two 2L CrI_3 , namely, between the 2nd and 3rd layers. Regions of AA (green), R (blue), and M-type (red) stacking geometries are marked in one moiré supercell (black parallelogram). Inset: schematic of twisting two 2L CrI_3 by an angle of α. **b.** The periodically modulating interlayer exchange coupling J at the interface between two 2L CrI_3. **c**–**e.** The calculated distributions of out-of-plane magnetization M_z in a moiré supercell for all four layers CrI_3 at three representative twist angles, $\alpha = 0.1^o$ (**c**), 1^o (**d**), and 10^o (**e**), with zero, nonzero, and zero total magnetization, respectively. **f**–**h.** The sketch of calculated layered magnetism centering at AA (green), across M (red), and centering at R (blue) sites for the magnetic ground states in **c**–**e**.

Figure 2. SAED and DF-TEM of high-quality moiré superlattice in tDB CrI_3. a. Electron diffraction pattern showing the Bragg peaks for the CrI_3 honeycomb lattice (marked by black circles) and the 2nd order moiré superlattice peaks (marked by blue circles). The measured twist angle is $\alpha = 1.4^o \pm 0.1^o$. **b.** DF-TEM images for each of the three pairs of Bragg and superlattice peaks, labeled by the corresponding Bragg peak indices. **c.** Composite image made by summing up the three DF-TEM images in (**b**) to show a uniform, high-quality superlattice. The red parallelogram indicates the moiré supercell.

Figure 3. Magnetic field dependent MCD data, model fits, and spin configurations for 1.1^o tDB CrI_3. a. MCD data and fits normalized to the MCD value at 2T taken at 10K under an out-of-plane magnetic field $B_\perp$ sweeping from + 2T to – 2T and then back to + 2T, for 1.1^o tDB, 2L, and 4L CrI_3. The spin flip transitions are marked by the black arrows in all three panels. The error bars correspond to one standard deviation of 15,000 MCD intensities measured over a time interval of 10 s at every magnetic field. The fitting model is detailed in Methods. **b** and **c.** Contributions from collinear and noncollinear spins to the MCD signal extracted from the model fits, in 1.1^o tDB, 2L, and 4L CrI_3. **d.** Schematics of M_z distribution evolving upon increasing $B_\perp$ from 0 T across B_{c1}^{tDB} to 2T.

Figure 4. Twist angle dependence of MCD data of tDB CrI_3. a. Normalized MCD data and fits taken at 10K under $B_\perp$ sweeping from + 2T to – 2T and then back to + 2T, for 4L, α = 0.5°, 1.1°, 2°, 5°, 10° tDB, and 2L CrI_3 (top panel). The hysteresis loops and spin flip transitions are marked in red shades and with black arrows, respectively. The error bars correspond to one standard deviation of 15,000 MCD intensities measured over a time interval of 10 s at every magnetic field. Contributions from the collinear (middle panel) and the noncollinear (bottom panel) spins are extracted from the model fitting. **b**–**f.** Twist angle dependence of the spin flip transition field B_{c1}, spin flip transition field width ΔB_{c1}, the slope at 0T

$\Delta\mathrm{MCD}/\Delta B_{\perp}$, the weight of the noncollinear spin contribution $W_{\mathrm{noncollinear}}$, and the net magnetization M_z^{tDB}, extracted from the model fitting. The error bars correspond to two standard error in fitting the MCD data.

Figure 5. Temperature dependence of the MCD and polarized Raman Scattering data of 1.1° tDB CrI_3. a. Normalized MCD data and fits at selected temperatures for 1.1° tDB CrI_3. Datasets are offset vertically for clarity. **b**–**f.** Temperature dependence of the normalized MCD value at 0T MCD(0T)/MCD(2T), the spin flip transition field B_{c1}, spin flip transition field width ΔB_{c1}, the slope at 0T $\Delta\mathrm{MCD}/\Delta B_{\perp}$, and the weight of the noncollinear spin contribution $W_{\mathrm{noncollinear}}$, extracted from the model fitting to MCD data of 1.1° tDB (blue circles), 2L (light purple circles), and 4L (light blue circles) CrI_3. The stripe shaded regions in **c**, **d**, and **f** correspond to the temperature range where these parameters are not defined in the fitting model. **g**. Polarized Raman Scattering spectra at selected temperatures for 1.1° tDB CrI_3 in the linearly parallel and crossed channels, showing the Davydov splitting induced layered-magnetism-assisted phonon modes $U_{1\text{-}4}$. **h**. Temperature dependence of the Raman mode $U_{2\text{-}4}$ arising from the layered AFM order in 1.1° tDB CrI_3[8]. The error bars correspond to two standard error in fitting the MCD/Raman spectra.

Methods

Fabrication of 2D natural CrI_3 and tDB CrI_3 The high-quality single crystals of CrI_3 were grown by the chemical vapor transport method, as reported in detail in Ref. [37]. Atomically thin CrI_3 films were mechanically exfoliated from bulk crystals onto 300 nm SiO_2/Si substrates inside a nitrogen-gas filled glovebox with both H_2O and O_2 level below 0.1 ppm. The thickness of CrI_3 flakes were initially identified by the optical contrast under an optical microscope inside the glovebox, and then further verified by the Raman spectroscopy at 10 K. Using the "tear-and-stack" technique, tDB CrI_3 samples were fabricated by initially picking up a part of 2L CrI_3 and then stacking it on top of the remaining part on the substrate at a targeted twist angle of α. Both tDB and 4L/2L CrI_3 were encapsulated on both sides with hexagonal boron nitride (hBN) flakes of $\sim$15 nm thick. The final stack of hBN/CrI_3/hBN was released onto the SiO_2/Si substrates and then rinsed in chloroform solvent to clean the polymer residue, before subsequent magneto-optical measurements.

Electron diffraction and transmission electron microscopy Selected area electron diffraction (SAED) and dark-field transmission electron microscopy (DF-TEM) results of tDB CrI_3 were acquired using Thermo Fisher Scientific Talos, equipped with Gatan OneView Camera. The twist angle was

quantified by fitting $(30\bar{3}0)$ Bragg peaks with two-dimensional Gaussians. DF-TEM in Figure 2b were acquired by achieving two-beam conditions on $(0\bar{3}30)$, $(\bar{3}300)$, $(30\bar{3}0)$ Bragg and satellite reflections. Figure 2c was generated by averaging the three DF-TEM micrographs in Fig. 2b to remove anisotropy.

Magnetic circular dichroism Similar MCD measurements were reported in atomically thin CrI_3 flakes in earlier studies. For the measurements in this current study, the normal incident light of a wavelength at 632.8 nm was focused onto the hBN/CrI_3/hBN sample with a full width at half maximum (FWHM) of 2-3 μm using a ×40 transmissive objective, which is substantially smaller than the sample sizes of both tDB and 4L/2L CrI_3. The polarization of the incident light was modulated between left- and right-handed circular polarizations (L/RCP) using the photo-elastic modulator (Hinds Instruments PEM-200) at a modulating frequency $f = 50$ kHz. The reflected signal was collected by a biased photodiode detector. Two separate measurements were carried out to determine the difference between and the average of the LCP and RCP light in the reflection. The difference was measured by demodulating the reflected signal against the PEM frequency using a lock-in amplifier. And the average was measured by inserting a mechanical chopper into the incident beam and then demodulating the reflected light at the mechanical chopper frequency with the lock-in amplifier. The MCD value was defined by the ratio of difference to average signal.

Polarized Raman spectroscopy Raman Scattering measurements were carried out using a 632.81 nm excitation laser with the FWHM value of 0.85 cm^{-1}, on the resonance with charge transfer and Cr^{3+} $^4A_2$ to $^4A_1$ transitions of CrI_3 to increase the Raman sensitivity. The laser beam on the sample site was focused down to ~ 2–3 μm FWHM in diameter using ×40 transmissive objective, and the laser power was kept at about 80 μW to minimize the local heating effect during measurements. Backscattering geometry was used, where the scattered light was dispersed by a Horiba LabRAM HR Evolution Raman microscope (grating with 1,800 grooves mm^{-1}) from Horiba Scientific and detected by a thermoelectrically cooled charge-coupled device camera from Horiba Scientific, with a spectrometer resolution of 0.3 cm^{-1}. A commercial variable-temperature (<10–325 K), closed-cycle microscopy cryostat (Cryo Industries of America) was interfaced with the Raman microscope.

Calculations of magnetic ground state of tDB CrI_3 We include the intralayer exchange coupling, the spin anisotropy energy, the interlayer AFM exchange coupling within each bilayer, and the modulated interlayer exchange coupling between the two bilayers in the magnetic Hamiltonian

$$H = \sum_{l=1}^{4} H^{(l)} + H_M^{(1,2)} + H_{\text{Moiré}}^{(2,3)} + H_M^{(3,4)} \quad (1)$$

For the twist angles that we consider (*e.g.*, intermediate twist angles, for example, ~1°), the moiré wavelength is about ~ 40nm, and magnetization in each layer varies slowly in real space. Therefore, we can take the continuum limit of the following spin Hamiltonian:

$$H = J_{\text{intra}} \sum_{<i,j>} (S_i^x S_j^x + S_i^y S_j^y + \gamma\, S_i^z S_j^z) \tag{2}$$

where $< i, j >$ represents a pair of nearest-neighbor Cr^{3+} ions, $J_{\text{intra}} \approx -2.2$ meV/μ_B^2 [27]is the effective spin exchange constant, and $\gamma = 1.0445$ [38] is the spin anisotropy constant. If we ignore quantum fluctuations, the spin vector on site i can be represented as $\boldsymbol{S_i} = S\, \boldsymbol{n_i}$, where $\boldsymbol{n_i} = (n_{i,x}, n_{i,y}, n_{i,z})$ is a 3D unit vector and $S = \frac{3}{2}\mu_B$ for Cr^{3+} ions. Thus, the intralayer Hamiltonian can be written as

$$H = J_{\text{intra}} S^2 \sum_{<i,j>} (n_{i,x} n_{j,x} + n_{i,y} n_{j,y} + \gamma\, n_{i,z} n_{i,z}) \tag{3}$$

If magnetization varies slowly in the real space, we can take the continuum limit, replacing $\boldsymbol{n_i}$ with a smooth function $\boldsymbol{n}(\boldsymbol{r})$, which is also a 3D unit vector

$$H = J_{\text{intra}} S^2 \sum_{<i,j>} [n_x(\boldsymbol{r_i}) n_x(\boldsymbol{r_j}) + n_y(\boldsymbol{r_i}) n_y(\boldsymbol{r_j}) + \gamma\, n_z(\boldsymbol{r_i}) n_z(\boldsymbol{r_j})] \tag{4}$$

In this continuum limit, we can perform a Tayler expansion, using $\boldsymbol{\delta r} = \boldsymbol{r_j} - \boldsymbol{r_i}$ as a small parameter

$$n_m(\boldsymbol{r_i}) n_m(\boldsymbol{r_j}) = n_m(\boldsymbol{r_i})^2 + n_m(\boldsymbol{r_i})\, \boldsymbol{\delta r} \cdot \nabla\, n_m(\boldsymbol{r_i}) + \frac{1}{2} n_m(\boldsymbol{r_i})\, (\boldsymbol{\delta r} \cdot \nabla)^2\, n_m(\boldsymbol{r_i}) + O(\delta r^3) \tag{5}$$

with $m = x, y,$ or z. Because the anisotropy factor $\gamma = 1.0445$ is close to 1 in CrI_3, here we take the following approximation. In the leading order term of this Taylor series, $n_m(r_i)^2$, we keep $\gamma = 1.0445$, while for higher order terms, we set $\gamma = 1$. This approximation simplifies the Hamiltonian without changing any qualitative features (i.e., we use n^2 terms to describe the easy-axis spin anisotropy of CrI_3, while derivative terms of $\boldsymbol{n}(\boldsymbol{r})$ preserve the SU(2) spin rotational symmetry). Within this approximation, the above Hamiltonian becomes

$$H = J_{\text{intra}} S^2 \sum_{\text{unit cells}} [3(n_x^2 + n_y^2 + \gamma\, n_z^2) - \frac{3}{4} \delta r^2 |\nabla \boldsymbol{n}|^2] \tag{6}$$

Here, first order derivate terms cancel out, while the second order derivative terms can be written as $\propto |\nabla \boldsymbol{n}|^2 = \sum_{a=x,y} \sum_{b=x,y,z} (\partial_a n_b)^2$. Higher order terms beyond $O(\delta r^2)$ are ignored. For the honeycomb lattice of Cr^{3+} ions, $\delta r = a/\sqrt{3}$, where a is the lattice constant, and the sum in the Hamiltonian above (over unit cells) can be replaced by the real space integral $\frac{1}{\mathcal{A}} \iint dx\, dy$, where $\mathcal{A} = \frac{\sqrt{3}}{2} a^2$ is the area of one unit cell. Thus, for each layer, the Hamiltonian becomes

$$H^{(l)} = \frac{J_{\text{intra}} S^2}{\mathcal{A}} \iint dx\, dy\, [-\frac{a^2}{4} \left|\nabla \boldsymbol{n}^{(l)}\right|^2 + 3({n_x^{(l)}}^2 + {n_y^{(l)}}^2 + \gamma\, {n_z^{(l)}}^2)] \tag{7}$$

where $l = 1,2,3,4$ is the layer index of the 4 layers.

For interlayer couplings, $H_M^{(1,2)}$ and $H_M^{(3,4)}$ describe the interlayer exchange interactions within each bilayer between layers (1,2) and layers (3,4)

$$H_{\mathrm{M}}^{(1,2)} = \frac{2\,J_M S^2}{\mathcal{A}} \iint dx\,dy\ \boldsymbol{n}^{(1)} \cdot \boldsymbol{n}^{(2)} \tag{8}$$

$$H_{\mathrm{M}}^{(3,4)} = \frac{2\,J_M S^2}{\mathcal{A}} \iint dx\,dy\ \boldsymbol{n}^{(3)} \cdot \boldsymbol{n}^{(4)} \tag{9}$$

where $J_M \approx 0.04\ \mathrm{meV}/\mu_B^2$ [27] is the effective AFM type interlayer exchange coupling constant between pristine monoclinically-stacked two layers.

$H_{\mathrm{Moiré}}^{(2,3)}$ denotes the periodically modulated magnetic coupling at the twisted interface between layers (2,3)

$$H_{\mathrm{Moiré}}^{(2,3)} = \iint dx\,dy \frac{2\,J_{\mathrm{Moiré}} S^2}{\mathcal{A}}\ \boldsymbol{n}^{(2)} \cdot \boldsymbol{n}^{(3)} \tag{10}$$

The moiré modulating interlayer exchange interaction $J_{\mathrm{Moiré}}$ takes the spatial distribution as shown in Figure 1b, which is obtained by adopting the interlayer exchange coupling at a few specific stacking sites [27] and then using the harmonic-regression up to the 2nd order to generate the two-dimensional spatial dependence, in analogy to the BM model [39].

To obtain the lowest-energy spin configuration in this continuous model, we discretize a Moiré unit cell using a triangular grid of $L \times L \times 4 = 60 \times 60 \times 4$, and define the following effective Hamiltonian on this grid

$$H^{(l)} = \frac{J_{intra} S^2}{3} \sum_{<i,j>} \boldsymbol{n_i^{(l)}} \cdot \boldsymbol{n_j^{(l)}} + \frac{3 J_{intra} S^2}{(\alpha L)^2} \sum_i [n_{ix}^{(l)^2} + n_{iy}^{(l)^2} + \gamma\, n_{iz}^{(l)^2}] \tag{11}$$

$$H_{\mathrm{M}}^{(1,2)} = \frac{2 J_M S^2}{(\alpha L)^2} \sum_i \boldsymbol{n_i^{(1)}} \cdot \boldsymbol{n_i^{(2)}} \tag{12}$$

$$H_{\mathrm{M}}^{(3,4)} = \frac{2 J_M S^2}{(\alpha L)^2} \sum_i \boldsymbol{n_i^{(3)}} \cdot \boldsymbol{n_i^{(4)}} \tag{13}$$

$$H_{\mathrm{Moiré}}^{(2,3)} = \sum_i \frac{2 J_{Moiré} S^2}{(\alpha L)^2}\ \boldsymbol{n_i^{(2)}} \cdot \boldsymbol{n_i^{(3)}} \tag{14}$$

where α is the twist angle and $L = 60$ is the linear size of grid that we use to discretize a moiré unit cell. The dimensionless quantity $(\alpha L)^2 = \mathcal{A}/\mathcal{A}_0$, where $\mathcal{A}$ and $\mathcal{A}_0$ are the areas of a CrI_3 unit cell and a unit cell of this triangular grid, respectively. It is straightforward to verify that this triangular grid model recovers the same continuous model shown above, and thus when L is sufficiently large, we can use this coarse-grained triangular grid to obtain the spin configuration of a moiré unit cell.

We then minimize this Hamiltonian via the quasi-Newton method. We allowed all spins in the four layers to vary in search of the ground state configuration. In addition, to avoid local energy minima, we examined a variety of initial conditions of spin arrangement, including (1) fully random, (2) largely homogenous in all four layers, (3) largely homogenous in some of the layers (random in others). We then identify the final state with the lowest energy by comparing results from different initial conditions. We note that the lowest-energy state is highly robust and always exhibit the same spin configuration (up to the degenerate states related by the spontaneous broken symmetries), and that these lowest-energy states can always be accessed from the fully random initial conditions.

The resulting ground state depends on the competition between intralayer and interlayer energy, which depend on the twist angle differently. To see this in our model, the intralayer energy cost happen at the neighboring in-plane region between spins of opposite directions, captured by the first term in Eq. (7), $-\frac{J_{\text{intra}}a^2S^2}{4\mathcal{A}}\iint dx\,dy\left|\nabla \boldsymbol{n}^{(l)}\right|^2$, which scales to the area of the "transitioning" region between two regions with opposite spin alignments, i.e., $2\pi a_{\text{M}}\cdot d$ with a_{M} being moiré wavelength and d being the width of the "transitioning" region (the noncollinear spin region). According to Eq. (7), the comparison between first term and the second term provides the width d that is twist angle independent. The moiré wavelength a_{M}, on the other hand, is proportional to α^{-1} with α being the twist angle. The interlayer energy cost happens in the interface between layers in Eqs. (8), (9), and (10) whose energy all scales with the area of moiré cells, i.e., πa_{M}^2, proportional to α^{-2}. The different scaling leads to changes of the magnetic ground state as the twist angle changes.

Fitting model for MCD data Based on the observation of the MCD data, we find that for a typical 1.1° tDB CrI_3 measured below T_N, MCD data consist of two components: 1) the sharp spin flip component with critical fields at $\pm B_{c1}^{\text{tDB}}$ from the collinear spins; 2) the slow-varying component between -2 T to $+2$ T from the noncollinear spins.

For the collinear spin contribution, the out-of-plane spins take two possible directions, spin up and down, i.e., $\mu=\pm 2\cdot\frac{3}{2}\mu_B$. Boltzmann statistics dictates that the mean magnetization under an external field B follows the *tanh* function

$$<\mu>=\frac{3\mu_B e^{\frac{3\mu_B B}{k_B T}}-3\mu_B e^{-\frac{3\mu_B B}{k_B T}}}{e^{\frac{3\mu_B B}{k_B T}}+e^{-\frac{3\mu_B B}{k_B T}}}\sim \tanh\frac{3\mu_B}{k_B T}B$$

Based on the system equivalency under time-reversal operation for the collinear spins as we observed from the natural 2L/4L CrI_3, the spin-flip transitions adopt two constraints: 1) "flip-up" and "flip-down" transitions should occur at the same magnetic field strength despite opposite magnetic field directions; 2) the increasing-field curve and the decreasing-field curve should map to each other by inversing about the origin at $x = 0$ and $y = 0$ (i.e., $B_\perp = 0$ and MCD = 0 in the MCD spectra).

For the noncollinear spin contribution, phenomenologically we also take a *tanh* function with a wide width to describe the slow-varying feature. Yet, no constraints were added, unlike the collinear spin contributions.

As a result, the following model is used to fit the MCD curve

$$\begin{cases} y_+ = A_{\mathrm{neg}} \tanh\dfrac{x+B}{C} + A_{\mathrm{pos}} \tanh\dfrac{x-B}{C} + a_+ \tanh\dfrac{x-b_+}{c_+} \\ y_- = A_{\mathrm{pos}} \tanh\dfrac{x+B}{C} + A_{\mathrm{neg}} \tanh\dfrac{x-B}{C} + a_- \tanh\dfrac{x-b_-}{c_-} \end{cases}$$

where x is the external magnetic field $B_\perp$, $y_{+(-)}$ is the MCD signal in an increasing(decreasing)-field measurement. For each equation, the first two terms explain the spin-flip transitions of Ising spins and the third term represents the response of the noncollinear spins. $A_{\mathrm{neg(pos)}}$ describes the magnitude of the spin-flip transition, B and C are the transition field B_{c1} and width ΔB_{c1}, respectively, for the collinear part. Those parameters are kept common in fitting y_+ and y_- datasets to fulfill the two aforementioned constrains for the collinear spins. For the noncollinear contribution, $a_\pm$, $b_\pm$, $c_\pm$ describe the magnitude, center and width of the slow-varying background in either an increasing$(+)$ or decreasing$(-)$ measurement and are independent between the increasing and decreasing field traces. For this emergent noncollinear contribution, we choose to release the time-reversal operation related constraints between data of increasing and decreasing B field and check from the fitted results whether the corresponding fitting parameters are indeed the same between up and down sweeps.

Data availability

All data shown in the main text and supplementary materials are available upon reasonable request from the corresponding authors (R.He. & L.Z.).

Acknowledgements

We thank Nishkarsh Agarwal for helpful discussions and assistance in SAED and DF-TEM measurements. L.Z. acknowledges support by NSF CAREER grant no. DMR-174774, AFOSR YIP grant no. FA9550-21-1-0065, and Alfred P. Sloan Foundation. R.He. acknowledges support by NSF grant no. DMR-2104036 and NSF CAREER grant No. DMR-1760668. R.Hovden. acknowledges support from ARO grant no. W911NF-22-1-0056. S.H.S. acknowledges support from the W.M. Keck Foundation. K.S. acknowledges support by NSF grant no. NSF-EFMA-1741618. H.L. acknowledges support by the National Key R&D Program of China (grant nos. 2018YFE0202600 and 2016YFA0300504), the Beijing Natural Science Foundation (grant no. Z200005), and the Fundamental Research Funds for the Central Universities and Research Funds of Renmin University of China (grant nos. 18XNLG14, 19XNLG17 and 20XNH062).

Author contributions

L.Z., H.X., and X.L. conceived the idea and initiated this project. H.X. and Z.S. fabricated the 4L, 2L, and tDB CrI_3 samples. H.X., X.L., Z.Y., G.Y. and H.G. built the MCD setup and carried out the MCD measurements under the supervision of L.Z. and R. He. S.H.S. and R. Hovden performed the electron diffraction and TEM measurements. S.Y., Y.F., S.T., and H.L. grew the CrI_3 bulk single crystals. X.L. and K.S. performed the theoretical computation and analysis. X.L. and L.Z. analyzed the data, and X.L., R.He, and L.Z. wrote the manuscript. All authors participated in the discussion of the results.

Competing interests

The authors declare that they have no competing interests.

References

1 Andrei, E. Y. *et al.* The marvels of moiré materials. *Nature Reviews Materials* **6**, 201-206, doi:10.1038/s41578-021-00284-1 (2021).
2 Kennes, D. M. *et al.* Moiré heterostructures as a condensed-matter quantum simulator. *Nature Physics* **17**, 155-163 (2021).
3 Hejazi, K., Luo, Z.-X. & Balents, L. Noncollinear phases in moiré magnets. *Proceedings of the National Academy of Sciences* **117**, 10721-10726, doi:10.1073/pnas.2000347117 (2020).
4 Hejazi, K., Luo, Z.-X. & Balents, L. Heterobilayer moiré magnets: Moiré skyrmions and commensurate-incommensurate transitions. *Physical Review B* **104**, L100406, doi:10.1103/PhysRevB.104.L100406 (2021).

5 Tong, Q., Liu, F., Xiao, J. & Yao, W. Skyrmions in the Moiré of van der Waals 2D Magnets. *Nano Letters* **18**, 7194-7199, doi:10.1021/acs.nanolett.8b03315 (2018).

6 Akram, M. & Erten, O. Skyrmions in twisted van der Waals magnets. *Physical Review B* **103**, L140406, doi:10.1103/PhysRevB.103.L140406 (2021).

7 Akram, M. *et al.* Moiré Skyrmions and Chiral Magnetic Phases in Twisted CrX3 (X = I, Br, and Cl) Bilayers. *Nano Letters* **21**, 6633-6639, doi:10.1021/acs.nanolett.1c02096 (2021).

8 Xie, H. *et al.* Twist engineering of the two-dimensional magnetism in double bilayer chromium triiodide homostructures. *Nature Physics* **18**, 30-36, doi:10.1038/s41567-021-01408-8 (2022).

9 Xu, Y. *et al.* Coexisting ferromagnetic–antiferromagnetic state in twisted bilayer CrI_3. *Nature Nanotechnology* **17**, 143-147, doi:10.1038/s41565-021-01014-y (2022).

10 Song, T. *et al.* Direct visualization of magnetic domains and moiré magnetism in twisted 2D magnets. *Science* **374**, 1140-1144, doi:10.1126/science.abj7478 (2021).

11 Nakatsuji, S., Kiyohara, N. & Higo, T. Large anomalous Hall effect in a non-collinear antiferromagnet at room temperature. *Nature* **527**, 212-215, doi:10.1038/nature15723 (2015).

12 Kimura, T. Spiral Magnets as Magnetoelectrics. *Annual Review of Materials Research* **37**, 387-413, doi:10.1146/annurev.matsci.37.052506.084259 (2007).

13 Yokouchi, T. *et al.* Emergent electromagnetic induction in a helical-spin magnet. *Nature* **586**, 232-236, doi:10.1038/s41586-020-2775-x (2020).

14 Fert, A., Reyren, N. & Cros, V. Magnetic skyrmions: advances in physics and potential applications. *Nature Reviews Materials* **2**, 17031, doi:10.1038/natrevmats.2017.31 (2017).

15 Liang, T. *et al.* Orthogonal magnetization and symmetry breaking in pyrochlore iridate $Eu_2Ir_2O_7$. *Nature Physics* **13**, 599-603, doi:10.1038/nphys4051 (2017).

16 Gong, C. & Zhang, X. Two-dimensional magnetic crystals and emergent heterostructure devices. *Science* **363**, eaav4450, doi:10.1126/science.aav4450 (2019).

17 Burch, K. S., Mandrus, D. & Park, J.-G. Magnetism in two-dimensional van der Waals materials. *Nature* **563**, 47-52, doi:10.1038/s41586-018-0631-z (2018).

18 Mak, K. F., Shan, J. & Ralph, D. C. Probing and controlling magnetic states in 2D layered magnetic materials. *Nature Reviews Physics* **1**, 646-661, doi:10.1038/s42254-019-0110-y (2019).

19 Huang, B. *et al.* Emergent phenomena and proximity effects in two-dimensional magnets and heterostructures. *Nature Materials* **19**, 1276-1289, doi:10.1038/s41563-020-0791-8 (2020).

20 Gibertini, M., Koperski, M., Morpurgo, A. F. & Novoselov, K. S. Magnetic 2D materials and heterostructures. *Nature Nanotechnology* **14**, 408-419, doi:10.1038/s41565-019-0438-6 (2019).

21 Wang, Q. H. *et al.* The Magnetic Genome of Two-Dimensional van der Waals Materials. *ACS Nano*, doi:10.1021/acsnano.1c09150 (2022).

22 Chen, L. *et al.* Magnetic anisotropy in ferromagnetic CrI_3. *Physical Review B* **101**, 134418, doi:10.1103/PhysRevB.101.134418 (2020).

23 Huang, B. *et al.* Layer-dependent ferromagnetism in a van der Waals crystal down to the monolayer limit. *Nature* **546**, 270-273, doi:10.1038/nature22391 (2017).

24 Li, S. *et al.* Magnetic-Field-Induced Quantum Phase Transitions in a van der Waals Magnet. *Physical Review X* **10**, 011075, doi:10.1103/PhysRevX.10.011075 (2020).

25 Li, T. *et al.* Pressure-controlled interlayer magnetism in atomically thin CrI_3. *Nature Materials* **18**, 1303-1308, doi:10.1038/s41563-019-0506-1 (2019).

26 Song, T. *et al.* Switching 2D magnetic states via pressure tuning of layer stacking. *Nature Materials* **18**, 1298-1302, doi:10.1038/s41563-019-0505-2 (2019).

27 Sivadas, N., Okamoto, S., Xu, X., Fennie, C. J. & Xiao, D. Stacking-Dependent Magnetism in Bilayer CrI_3. *Nano Letters* **18**, 7658-7664, doi:10.1021/acs.nanolett.8b03321 (2018).

28 Wang, C., Gao, Y., Lv, H., Xu, X. & Xiao, D. Stacking Domain Wall Magnons in Twisted van der Waals Magnets. *Physical Review Letters* **125**, 247201, doi:10.1103/PhysRevLett.125.247201 (2020).

29 Jiang, P. *et al.* Stacking tunable interlayer magnetism in bilayer CrI_3. *Physical Review B* **99**, 144401, doi:10.1103/PhysRevB.99.144401 (2019).

30 Sung, S. H. *et al.* Torsional periodic lattice distortions and diffraction of twisted 2D materials. *Nature Communications* **13**, 7826, doi:10.1038/s41467-022-35477-x (2022).
31 Jin, W. *et al.* Tunable layered-magnetism–assisted magneto-Raman effect in a two-dimensional magnet CrI_3. *Proceedings of the National Academy of Sciences* **117**, 24664-24669, doi:10.1073/pnas.2012980117 (2020).
32 Song, T. *et al.* Giant tunneling magnetoresistance in spin-filter van der Waals heterostructures. *Science* **360**, 1214-1218, doi:10.1126/science.aar4851 (2018).
33 Marchiori, E. *et al.* Nanoscale magnetic field imaging for 2D materials. *Nature Reviews Physics* **4**, 49-60, doi:10.1038/s42254-021-00380-9 (2022).
34 Zhang, X.-X. *et al.* Gate-tunable spin waves in antiferromagnetic atomic bilayers. *Nature Materials* **19**, 838-842, doi:10.1038/s41563-020-0713-9 (2020).
35 Cenker, J. *et al.* Direct observation of two-dimensional magnons in atomically thin CrI_3. *Nature Physics* **17**, 20-25, doi:10.1038/s41567-020-0999-1 (2021).
36 Ghosh, A. *et al.* Intra-Atomic and Local Exchange Fields in the Van der Waals Magnet CrI_3. *arXiv preprint arXiv:2201.04400* (2022).
37 Jin, W. *et al.* Raman fingerprint of two terahertz spin wave branches in a two-dimensional honeycomb Ising ferromagnet. *Nature Communications* **9**, 5122, doi:10.1038/s41467-018-07547-6 (2018).
38 Kim, H. H. *et al.* Evolution of interlayer and intralayer magnetism in three atomically thin chromium trihalides. *Proceedings of the National Academy of Sciences* **116**, 11131-11136 (2019).
39 Bistritzer, R. & MacDonald, A. H. Moiré bands in twisted double-layer graphene. *Proceedings of the National Academy of Sciences* **108**, 12233-12237 (2011).

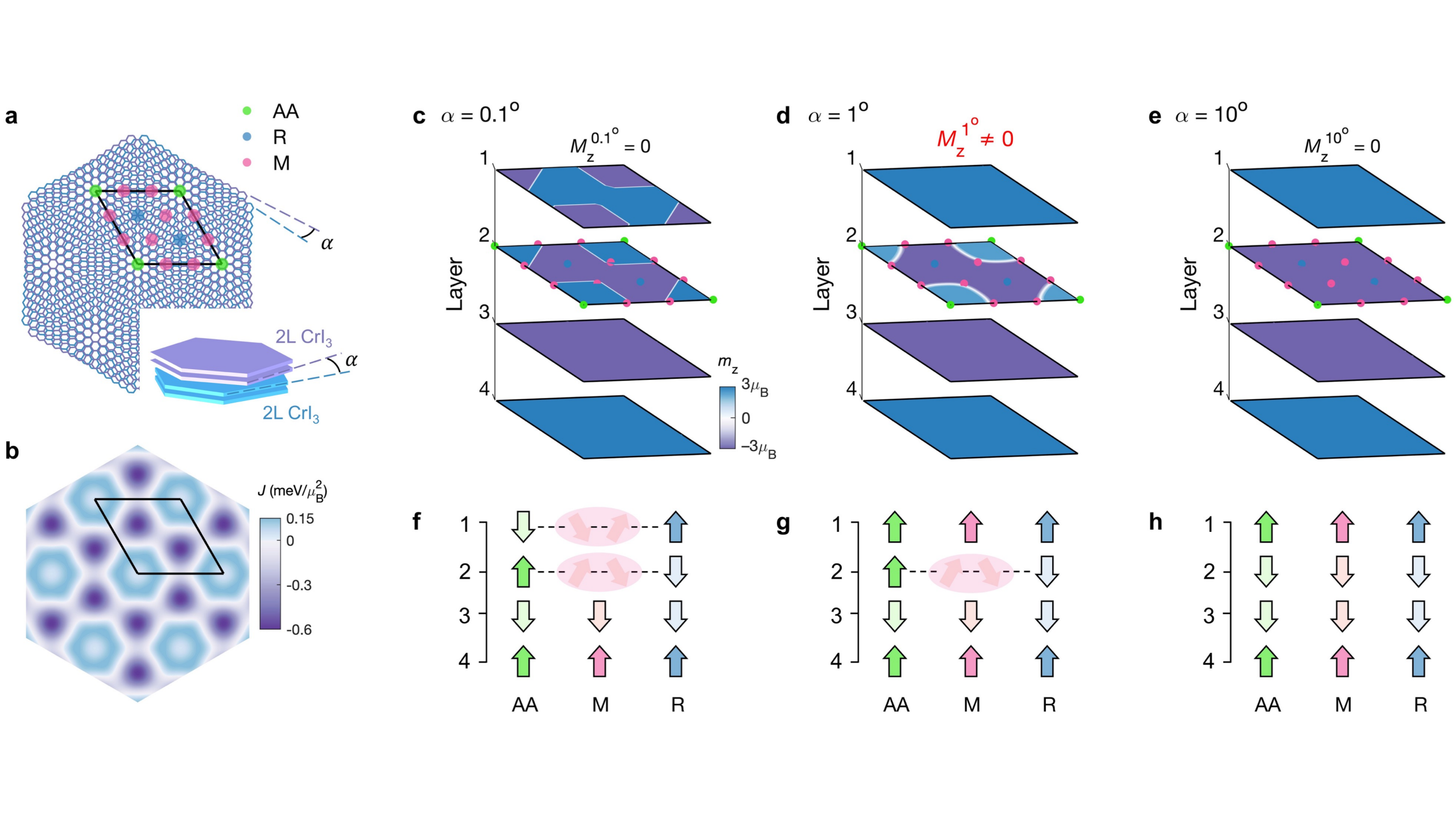
a
AA
R
M
α
2L CrI3
α
2L CrI3
b
J (meV/μB2)
0.15
0
-0.3
-0.6
c
α = 0.1°
M_z^0.1° = 0
Layer
1
2
3
4
m_z
3μB
0
−3μB
d
α = 1°
M_z^1° ≠ 0
Layer
1
2
3
4
e
α = 10°
M_z^10° = 0
Layer
1
2
3
4
f
1
2
3
4
AA
M
R
g
1
2
3
4
AA
M
R
h
1
2
3
4
AA
M
R

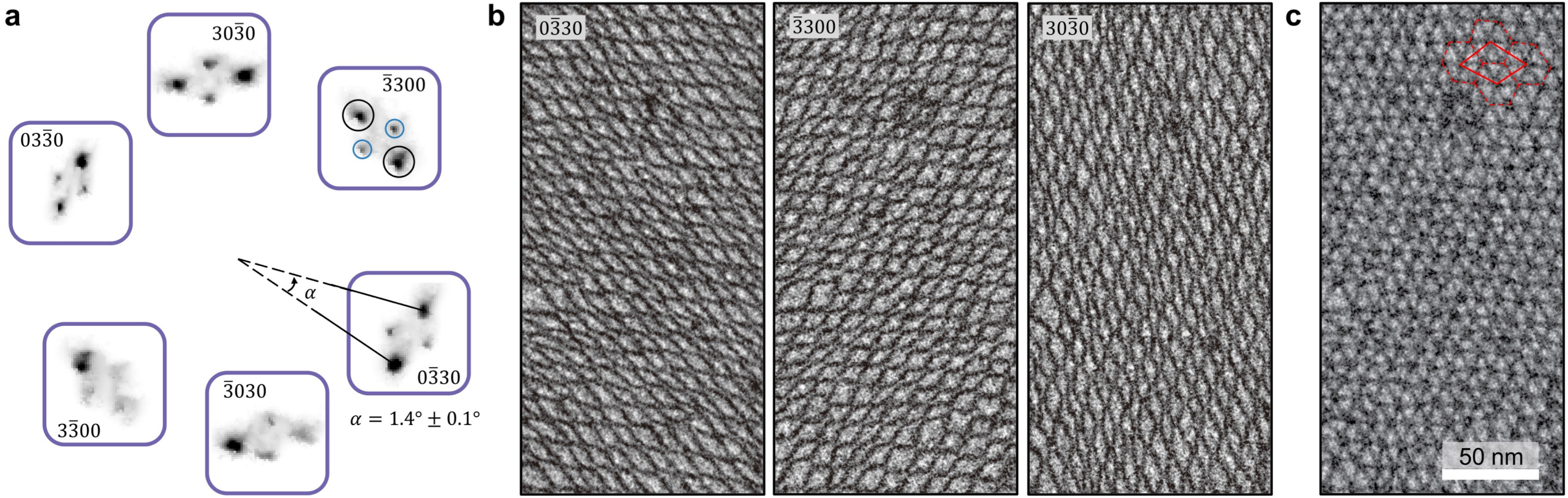
a
$30\bar{3}0$
$\bar{3}300$
$03\bar{3}0$
α
$3\bar{3}00$
$\bar{3}030$
$0\bar{3}30$
$\alpha = 1.4° \pm 0.1°$
b
$0\bar{3}30$
$\bar{3}300$
$30\bar{3}0$
c
50 nm

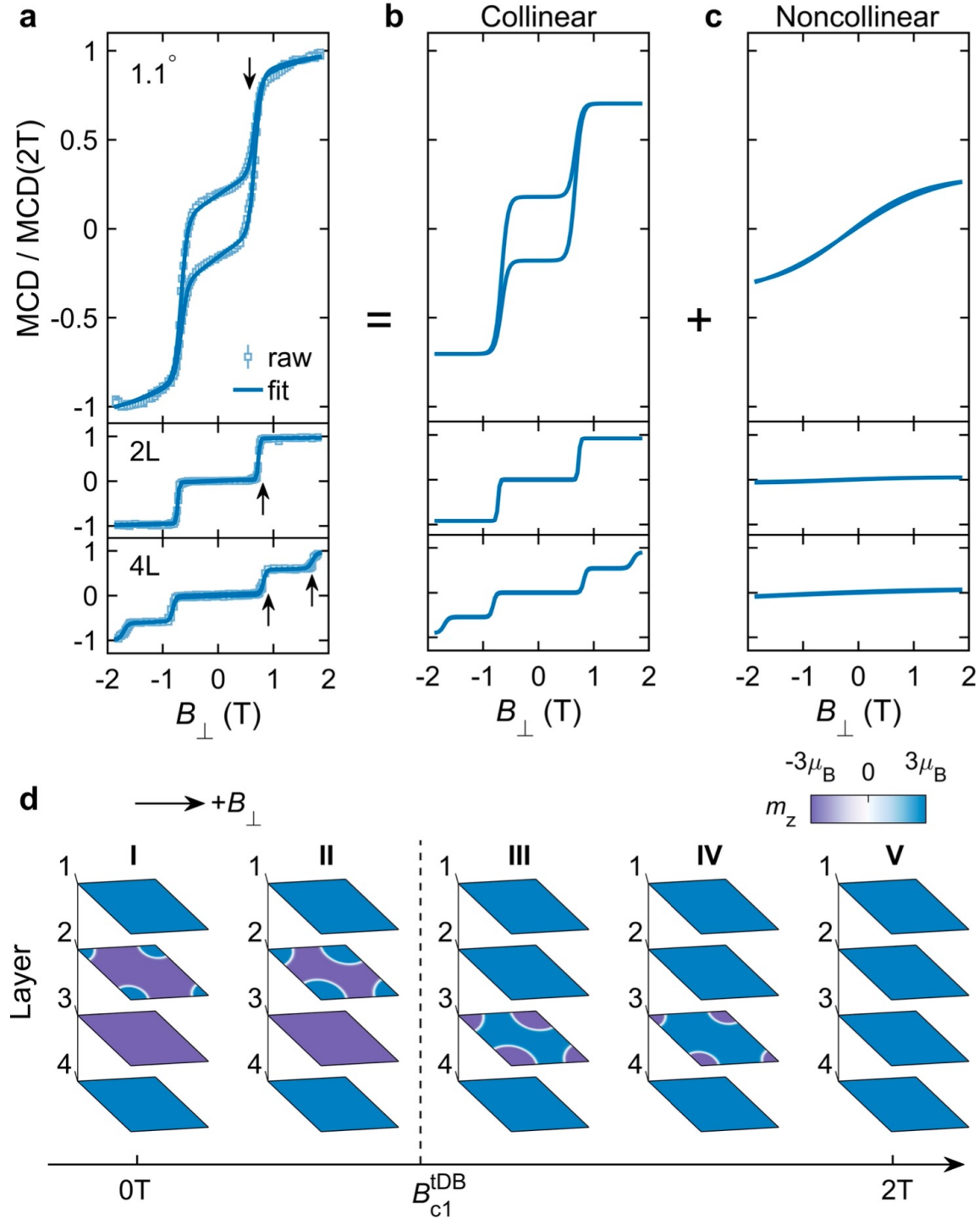
a
b
Collinear
c
Noncollinear
1.1°
MCD / MCD(2T)
raw
fit
2L
4L
=
+
$B_\perp$ (T)
d
$+B_\perp$
$-3\mu_B$ 0 $3\mu_B$
m_z
I
II
III
IV
V
Layer
0T
B_{c1}^{tDB}
2T

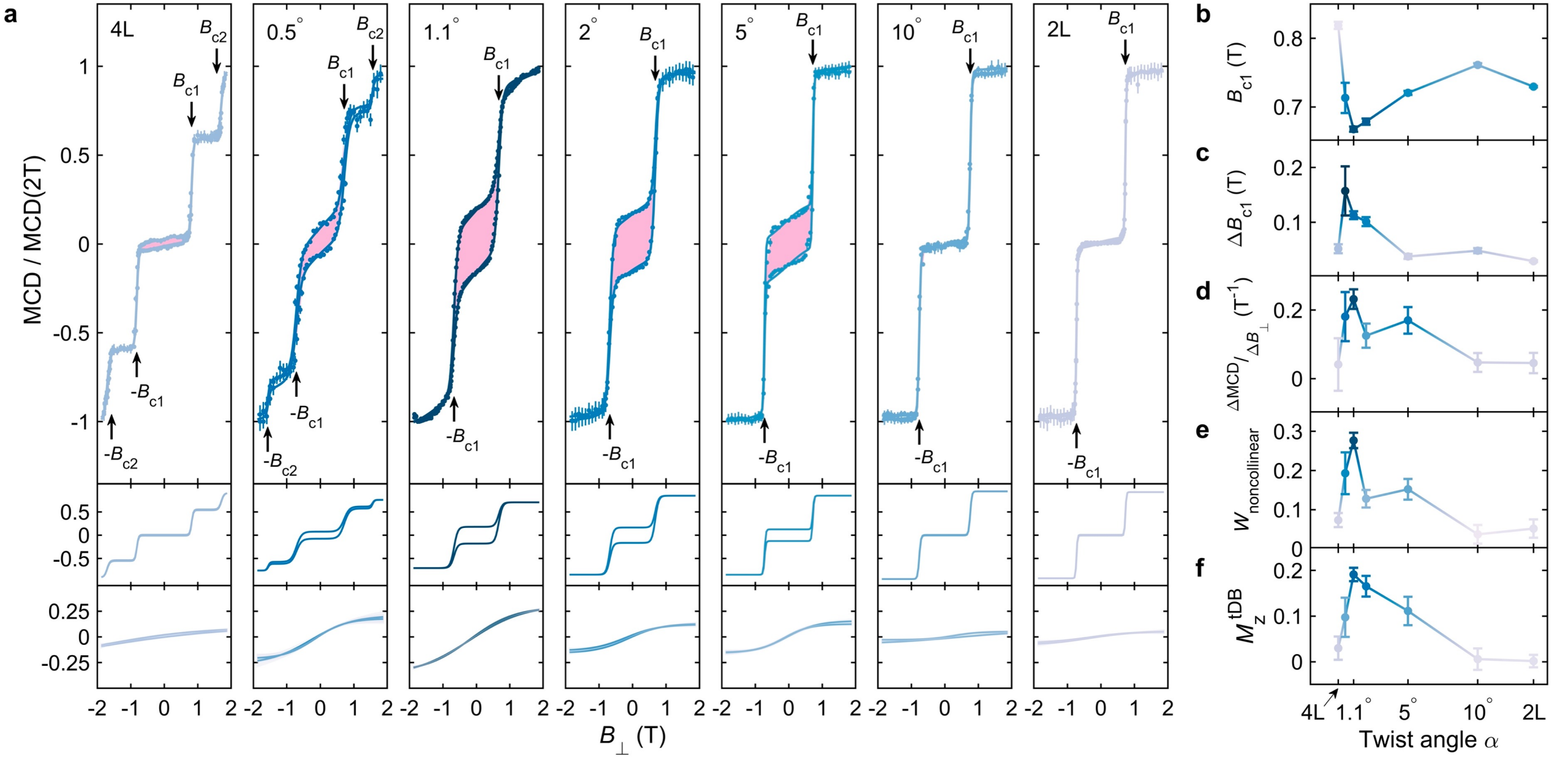
a
4L
0.5°
1.1°
2°
5°
10°
2L
B_{c2}
B_{c1}
$-B_{c2}$
$-B_{c1}$
MCD / MCD(2T)
$B_\perp$ (T)
b
B_{c1} (T)
c
ΔB_{c1} (T)
d
$\Delta MCD/\Delta B_\perp$ (T^{-1})
e
$W_{noncollinear}$
f
M_z^{tDB}
Twist angle α

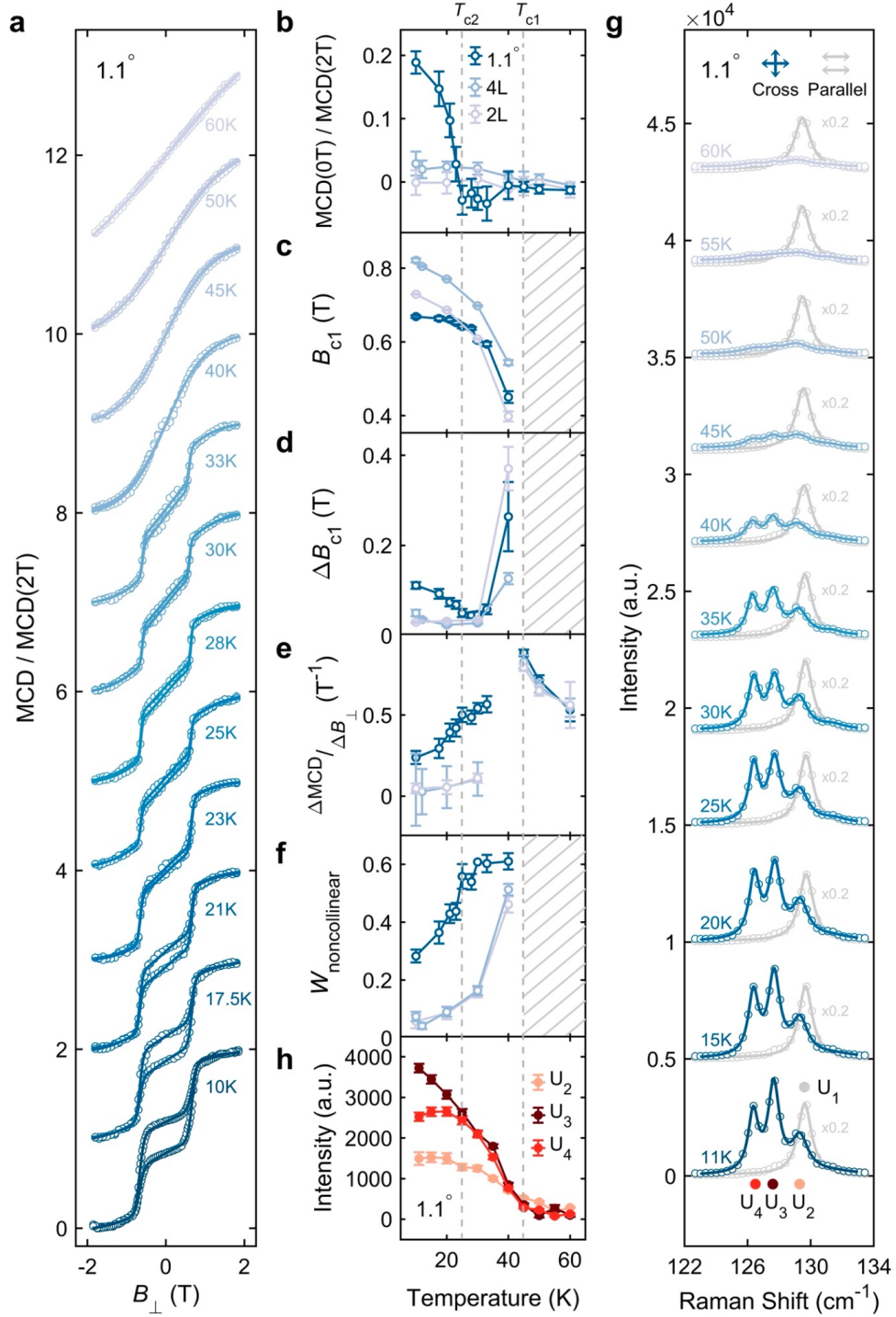
a
1.1°
60K
50K
45K
40K
33K
30K
28K
25K
23K
21K
17.5K
10K
MCD / MCD(2T)
$B_\perp$ (T)
b
T_{c2}
T_{c1}
1.1°
4L
2L
MCD(0T) / MCD(2T)
c
B_{c1} (T)
d
ΔB_{c1} (T)
e
$\Delta MCD / \Delta B_\perp$ (T^{-1})
f
$W_{noncollinear}$
h
Intensity (a.u.)
U_2
U_3
U_4
1.1°
Temperature (K)
g
$\times 10^4$
1.1°
Cross
Parallel
60K
55K
50K
45K
40K
35K
30K
25K
20K
15K
11K
x0.2
U_1
U_4 U_3 U_2
Intensity (a.u.)
Raman Shift (cm^{-1})